Ceramics

Estimation of gamma-rays, and fast and the thermal neutrons attenuation characteristics for bismuth tellurite and bismuth boro-tellurite glass systems

G. Lakshminarayana[1,*] , Imen Kebaili[2,3], M. G. Dong[4], M. S. Al-Buriahi[5], A. Dahshan[2,6], I. V. Kityk[7], Dong-Eun Lee[8,*], Jonghun Yoon[9,*], and Taejoon Park[10,*]

[1] *Intelligent Construction Automation Center, Kyungpook National University, 80, Daehak-ro, Buk-gu, Daegu 41566, Republic of Korea*

[2] *Department of Physics, Faculty of Science, King Khalid University, P.O. Box 9004, Abha, Saudi Arabia*

[3] *Laboratoire de Physique Appliquée, Groupe de Physique des Matériaux Luminescents, Département de Physique, Faculté des Sciences de Sfax, Université de Sfax, BP 1171, 3018 Sfax, Tunisia*

[4] *Department of Resource and Environment, Northeastern University, Shenyang 110819, China*

[5] *Department of Physics, Sakarya University, Sakarya, Turkey*

[6] *Department of Physics, Faculty of Science, Port Said University, Port Said, Egypt*

[7] *Institute of Optoelectronics and Measuring Systems, Faculty of Electrical Engineering, Czestochowa University of Technology, 17 Armii Krajowej Str., 42-200 Czestochowa, Poland*

[8] *School of Architecture and Civil Engineering, Kyungpook National University, 80, Daehak-ro, Buk-gu, Daegu 41566, Republic of Korea*

[9] *Department of Mechanical Engineering, Hanyang University, 55 Hanyangdaehak-ro, Ansan, Gyeonggi-do 15588, Republic of Korea*

[10] *Department of Robotics Engineering, Hanyang University, 55 Hanyangdaehak-ro, Ansan, Gyeonggi-do 15588, Republic of Korea*

ABSTRACT

Gamma-rays and fast and thermal neutron attenuation features of $(Bi_2O_3)_x$–$(TeO_2)_{(100-x)}$ (where x = 5, 8, 10, 12, and 15 mol%) and $[(TeO_2)_{0.7}–(B_2O_3)_{0.3}]_{(1-x)}$–$(Bi_2O_3)_x$ (where x = 0.05, 0.10, 0,15, 0.20, 0.25, and 0.3 mol%) glass systems have been explored and compared. For all samples, mass attenuation coefficients (μ/ρ) are estimated within 0.015–15 MeV photon energy range by MCNP5 simulation code and correlated with WinXCom results, which showed a satisfactory agreement between computed μ/ρ values by these both methods. Additionally, effective atomic number (Z_{eff}), effective electron density (N_{eff}), half-value layer (HVL), tenth-value layer (TVL), mean free path (MFP), total atomic cross-section (σ_a), and total electronic cross-section (σ_e) are calculated by utilizing μ/ρ values. The μ/ρ, Z_{eff}, and N_{eff} are energy dependent and have higher values at the lowest energy and smaller values at higher energies. Moreover, using the G–P fitting method as a function of penetration depth (up to 40 mfp) and incident photon energy (0.015–15 MeV range), exposure buildup factors (EBFs) and

Address correspondence to E-mail: gandham@knu.ac.kr; dolee@knu.ac.kr; yooncsmd@gmail.com; taejoon@hanyang.ac.kr

energy absorption buildup factors (EABFs) are evaluated. Both $85TeO_2$–$15Bi_2O_3$ (mol%) and $49TeO_2$–$21B_2O_3$–$30Bi_2O_3$ (mol%) samples, by possessing higher values of Z_{eff}, exhibit minimum EBF and EABF values. Highest μ/ρ, Z_{eff} values and lowest HVL, TVL, MFP values of $49TeO_2$–$21B_2O_3$–$30Bi_2O_3$ (mol%) sample indicated its better gamma-ray absorption capability among all selected glasses. Further, macroscopic effective removal cross-section for fast neutrons (Σ_R), coherent scattering cross-section (σ_{cs}), incoherent scattering cross-section (σ_{ics}), absorption cross-section (σ_A), and total cross-section (σ_T) values for thermal neutron attenuation have been computed. Among all samples, $49TeO_2$–$21B_2O_3$–$30Bi_2O_3$ (mol%) glass possesses a better Σ_R value for fast neutron attenuation, while the largest 'σ_T' value of $66.5TeO_2$–$28.5B_2O_3$–$5Bi_2O_3$ (mol%) sample suggests its good thermal neutron absorption efficiency.

Introduction

Nuclear technology with ionizing radiations is offering its contributions in nuclear power plants (producing electricity), outer space research, medical diagnostics and radiotherapy (nuclear medicine), agriculture, petroleum industry, food preservative and sterilization, especially with the help of continuous shielding and dosimetry. However, for such implementations, a photon–matter interaction or penetration study is an important research topic in the field of radiation physics. Such knowledge prevents the harsh radiations from causing serious damage to the equipment or tools and also helps in protecting living beings from exposure to dangerous X-rays and gamma radiations beyond acceptable dose levels [1]. Hence, developing efficient shielding materials to minimize the radiation exposure effects is a challenging task, nowadays. The challenge depends prevailingly upon the type and energy of the radiation. Any material, in principle, can be employed for X-rays, γ-rays, and neutron attenuation if it has an appropriate thickness to absorb and/or diffuse incident photons or neutrons to a safer level [2–4]. Also, the type of shielding material depends upon the application areas. The nuclear reactors require shielding against primary neutron beam and gamma-rays and transparent shielding materials for nuclear medicine. Therefore, materials, which possess excellent optical transparency and quality radiation attenuation parameters, are suitable candidates for protection against radiations. The mentioned dual qualities can be identified in optical glasses, unlike conventional concretes that are used as protective materials against radiations where concretes show demerits such as cracks formation in their structure with a prolonged radiations interaction, and they are non-transportable, heavy, and opaque to visible light [5]. Glasses could be used to attenuate potentially harmful radiations like gamma-rays, thereby using them as transparent radiation shields. Moreover, glass manufacturing is cost-effective, easily moldable, 100% recyclable capability, and glasses show high homogeneity and they are structurally, thermally, and mechanically stable depending upon the compositions, resulting in an attenuation efficacy [6–8]. Though, as radiation shields, lead (Pb)-based glasses or materials are being used at diagnostic imaging facilities, mainly 'Pb' element toxicity to the surrounding environment, working personnel, and cost restrict its usage. Thus, Pb-free, environmentally friendly, and non-toxic shielding glasses are required for their practical applications in medical and industrial fields. Further, for gamma radiation good shielding ability, and fast and thermal neutron beam absorption, glasses must possess high density, large atomic number, high absorption cross-section, and light elements in composition (e.g., B, Li) for an efficient elastic scattering. In this regard, heavy metal oxides (HMOs) such as Bi_2O_3 (density = 8.9 g/cm^3) and BaO (density = 5.72 g/cm^3)-based glasses are highly desirable due to their large effective atomic number (Z_{eff}), high density, and non-toxicity. Here, Bi_2O_3 closely matches PbO in density and γ-ray attenuation (strong absorption of gamma-rays), and due to weak field strength, Bi^{3+} ion cannot be viewed as a glass former. Here, compositions of the glasses play the principal role in shielding applications. The

weight fractions of glass systems are the prominent features of the attenuation effect. More the weight fraction of high atomic number and high-density elements in compositions, more the photons are attenuated.

For γ-rays attenuation characteristic study for any material, mass attenuation coefficient (μ/ρ) is an important physical parameter. Additionally, half-value layer (HVL), tenth-value layer (TVL), effective electron density (N_{eff}), effective atomic number (Z_{eff}), mean free path (MFP), exposure buildup factor (EBF), and energy absorption buildup factor (EABF) parameters are vital in understanding gamma radiation interaction through photoelectric absorption, Compton scattering, Rayleigh scattering, and pair production mechanisms with shielding material [6–9]. For the last few years, numerous research groups have been reported on gamma-ray shielding features of different glass systems using theoretical approaches and/or experimental methods.

Recently, for six different types of glasses composed of various metal oxides, μ/ρ, HVL, and exposure rate with and without buildup factors were reported by Waly et al. [10] using MicroShield software at low photon energies 15–300 keV, and they found that the 35 PbO + 55 Bi_2O_3 + 10 SiO_2 (wt%) glass shows the best μ/ρ, lowest exposure rate and HVL values among the other mixes. In other work, using WinXCom, Dong et al. [11] examined the gamma-ray shielding properties of ternary TeO_2–WO_3–PbO glasses in the 1 keV to 100 GeV energy range by calculating μ/ρ, Z_{eff}, and MFP values and found that 40 mol% PbO containing sample possesses superior γ-ray shielding. Tekin et al. [12] reported on the radiation shielding features (μ/ρ, Z_{eff}, HVL, and MFP) of B_2O_3–Bi_2O_3–SiO_2–TeO_2 -glasses at 356, 662, 1173, and 1332 keV photon energies utilizing MCNPX (version 2.4.0) code and found that the addition of Bi_2O_3 enhances the shielding ability of the samples. Kurudirek [13] investigated gamma, fast neutron, and charged particle interaction with heavy metal oxide borate (HMOB) glasses by deriving μ/ρ, Z_{eff}, Σ_R, and buildup factors and suggested that lead-free HMOB glasses are useful for γ-rays, fast neutrons, and heavy ion attenuation. Further, within the 0.015–15 MeV photon energy range and up to 40 mfp penetration depth, for $(75-x)B_2O_3$–xBi_2O_3–$10Na_2O$–$10CaO$–$5Al_2O_3$ $(0 \leq x \leq 25$ mol%) glasses, EBF and EABF values using the G–P fitting parameters method were reported by Al-Buriahi and Tonguc [14], and they identified that the 25 mol% of Bi_2O_3 containing sample shows the lowest EABF and EBF values for better γ-ray shielding ability. A comparative study on shielding properties of 21 tellurite glasses was reported by Mallawany et al. [15], evaluating the μ/ρ, Z_{eff}, HVL, and (Σ_R) values within 10 keV–10 MeV photon energy range by applying XCOM program, and they established that TeO_2–V_2O_5–CeO_2 glasses possess the highest $\sum_R$ value. Very recently, Siengsanoh et al. [16] studied xBaO–$5WO_3$–$15Na_2O$-($80-x$)B_2O_3 glasses ($x = 5, 10, 15, 20, 25, 30,$ and 35 mol%) radiation shielding properties using WinXCom program at the 1 keV to 100 GeV photon energy range and noticed that with BaO content increment, μ/ρ increases and thereby all the interactions such as photoelectric absorption, coherent, incoherent scattering, and pair production also increase.

Tellurite-rich glasses can be synthesized at low melting temperatures (< 1173 K) and possess promising features such as high refractive index (1.9–2.3), high dielectric permittivity, wide mid-infrared transmission region (0.25–6 μm), large third-order nonlinear optical (NLO) susceptibility, high rare-earth (RE) ion solubility, low cutoff phonon energy (~ 750 cm^{-1}), adequate chemical durability and thermal stability, better mechanical strength and high resistance to moisture [17]. Conversely, B_2O_3 is a traditional oxide glass former, which exhibits low cationic size (~ 41 pm) and high bond strength (~ 809 kJ/mol), could be prepared at low melting temperatures, and possesses low viscosity, excellent glass-forming ability, high optical transparency, and heat resistance including moderate RE ion solubility. However, B_2O_3 glasses show hygroscopic nature, low density (~ 2.5 g/cm^3), and high phonon energy (~ 1300–1500 cm^{-1}) [18]. Thus, boro-tellurite glasses demonstrate a combination of borate and tellurite qualities such as the ease of fabrication, enhanced UV transparency, moderate phonon energy, high chemical durability and thermal stability, and contains tetrahedral BO_4, trigonal BO_3, trigonal bipyramidal TeO_4, TeO_{3+1} polyhedra, and TeO_3 pyramidal structural units in their network [19, 20]. So, for example, compared with very recently reported other oxide glass systems such as alkali lead borate [21], lead borate + Bi_2O_3 [22], borosilicates + PbO [23], lead alumino-borate [24], and alkali borosilicates + PbO [25], bismuth tellurite and bismuth boro-tellurite

glasses that show non-toxic nature could be attractive for radiation shielding applications study.

In this work, for TeO$_2$–Bi$_2$O$_3$ and TeO$_2$–B$_2$O$_3$–Bi$_2$O$_3$ glass systems, (μ/ρ), Z_{eff}, N_{eff}, HVL, TVL, MFP, total atomic cross-section (ACS), and total electronic cross-section (ECS) as well as EBF, EABF have been evaluated at 0.015–15 MeV photon energy range including (Σ_R) and thermal neutron attenuation characteristics to explore their gamma-ray, fast neutron, and thermal neutron shielding efficiency. The μ/ρ values are derived using the MCNP5 code and WinXCom program. Using the G–P fitting method, EBF and EABF values are computed within the energy range 0.015–15 MeV as a function of MFP up to 40 mfp.

Materials and methods

The density values of five bismuth tellurite [chemical composition: (Bi$_2$O$_3$)$_x$–(TeO$_2$)$_{(100-x)}$ (x = 5, 8, 10, 12, and 15 mol%)] and six bismuth boro-tellurite [chemical composition: [(TeO$_2$)$_{0.7}$–(B$_2$O$_3$)$_{0.3}$]$_{(1-x)}$–(Bi$_2$O$_3$)$_x$ (x = 0.05, 0.10, 0,15, 0.20, 0.25, and 0.3 mol%)] glasses are taken from Refs. [26, 27]. Here, for convenience, bismuth tellurite and bismuth boro-tellurite glasses have been labeled as 'S1,' 'S2,' 'S3,' 'S4,' and 'S5' and 'P1,' 'P2,' 'P3,' 'P4,' 'P5,' and 'P6,' respectively. Tables 1 and 2 show each glass composition (in mol%) and their calculated elemental composition (in wt%) values for all selected bismuth tellurites and bismuth boro-tellurites. All the S1–S5 and P1–P6 samples, using the melt-quenching method, have been fabricated at 900 °C for 2 h and 900 °C for 1 h, respectively. Following the Archimedes principle, distilled water being an immersion liquid, all the glasses densities were determined. Here, the increasing density values from S1 → S5 and P1 → P6 samples refer to the substitution of lower-density TeO$_2$ (5.67 g/cm^3) and B$_2$O$_3$ (2.46 g/cm^3) chemicals

with higher-density Bi$_2$O$_3$ (8.9 g/cm^3) compound (Tables 1 and 2).

WinXCom program and MCNP5 code

WinXCom program [28], which depends on the web-based database, is user-friendly and easy to use to calculate 'μ/ρ' values for any mixture, compound, or element ($Z \leq 100$), within 1 keV–100 GeV photon energy. In this program, selected samples are defined by the constituent elemental fractions where incoherent and coherent scattering partial cross-sections, photoelectric absorption, pair production, total attenuation cross-section, and total 'μ/ρ' data are available for different elements. Later, users can choose particular γ-ray energy to compute the attenuation parameter value for a material.

Under the circumstances of inaccessibility to expensive equipment for determining experimentally the radiation shielding effectiveness of the selected various kinds of glass systems, performing general-purpose Monte Carlo (MC) simulations on these glasses is another best possibility to evaluate shielding parameters accurately. These MC simulations can be fully handled by widely used codes such as MCNP, Geant4, and FLUKA or others on a conventional desktop or laptop computer by defining gamma-ray sources, the detector, and the sample to be examined. The details on the MCNP5 simulation code that we used in this work within the 0.015–15 MeV photon energy range were the same as we described in our earlier works [29, 30]. For the utilized MCNP5 code, Fig. 1 shows the cross-sectional geometry setup. As a verification of the MCNP5 modeled geometry, the derived 'μ/ρ' values for both selected glass systems were compared with WinXCom results and % deviation between μ/ρ values is calculated using the below expression:

$$\%\text{Dev.} = \left| \left(\frac{\mu/\rho_{\text{WinXCOM}} - \mu/\rho_{\text{MCNP5}}}{\mu/\rho_{\text{WinXCOM}}} \right) \times 100 \right| \quad (1)$$

Table 1 Chemical composition (mol%) and elements (wt%) present in the selected bismuth tellurite glasses, including their density [26]

Glass code	Glass composition (mol%)		Elemental composition (wt%)			Density (g/cm^3)
	TeO$_2$	Bi$_2$O$_3$	Te	Bi	O	
S1	95	5	69.3015	11.9474	18.7511	5.43
S2	92	8	63.7627	18.1615	18.0757	5.69
S3	90	10	60.3675	21.9707	17.6617	5.85
S4	88	12	57.1841	25.5422	17.2736	6.03
S5	85	15	52.7650	30.5002	16.7347	6.26

Table 2 Chemical composition (mol%) and elements (wt%) present in the selected bismuth boro-tellurite glasses, including their density [27]

| Glass code	Glass composition (mol%)			Elemental composition (wt%)				Density (g/cm³)
	TeO₂	B₂O₃	Bi₂O₃	Te	B	Bi	O	
P1	66.5	28.5	5.0	56.8448	4.1281	13.9998	25.0270	4.29
P2	63.0	27.0	10.0	48.4438	3.5181	25.1873	22.8507	4.81
P3	59.5	25.5	15.0	41.5764	3.0193	34.3325	21.0716	5.20
P4	56.0	24.0	20.0	35.8578	2.6040	41.9479	19.5902	5.56
P5	52.5	22.5	25.0	31.0219	2.2528	48.3877	18.3374	5.85
P6	49.0	21.0	30.0	26.8792	1.9520	53.9046	17.2642	6.24
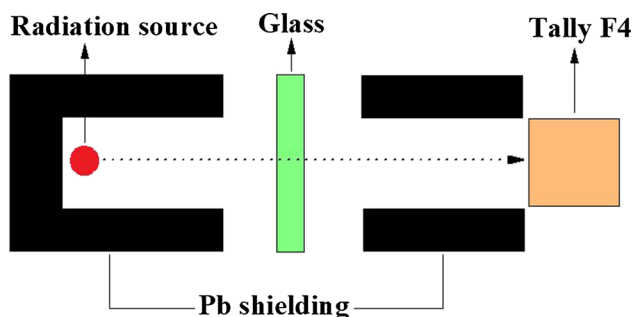
Figure 1 Total simulation geometry setup for MCNP5 to calculate μ/ρ values.

Computation of γ-ray attenuation parameters

The usual definitions and related formulae for γ-ray shielding parameters: (μ/ρ), Z_{eff}, N_{eff}, HVL, TVL, MFP, ACS, and ECS can be found elsewhere [2, 6–8, 20, 24, 25, 30, 31]. However, from 2.2.1 to 2.2.6 subsections, the relevant formulae that we used in this work are given for readers' convenience.

Mass attenuation coefficient (μ/ρ)

Following Beer–Lambert law, the μ/ρ of glass can be deduced by the following expressions:

$$I = I_0 e^{-\mu t} \quad (2)$$

and mixture rule

$$(\mu/\rho)_{glass} = \sum_i w_i (\mu/\rho)_i \quad (3)$$

where I_0 = initial photon intensity, I = transmitted photon intensity, μ (cm⁻¹) = linear attenuation coefficient, t (cm) = sample thickness, μ/ρ (cm²/g) = mass attenuation coefficient,

ρ (g/cm³) = glass density, w_i = weight fraction of ith element and '$(\mu/\rho)_i$' = mass attenuation coefficient of 'ith' constituent element in the glass. Here, the 'I/I_0' ratio is called the transmission factor.

Generally, during γ-ray interaction with materials, 'μ' represents the sum of three possibilities:

$$\mu = \tau(\text{photoelectric}) + \sigma(\text{Compton}) + \kappa(\text{pair}) \quad (4)$$

At low photon energies, mainly the photoelectric (PE) effect prevails, even though Compton scattering (CS), Rayleigh scattering (RS), and photonuclear absorption also take part. The CS occurs between photon and electron, while pair production (PP) takes place between a photon and a nucleus.

Effective atomic number (Z_{eff})

The Z_{eff} of materials can be obtained from μ/ρ values as stated in the below relation:

$$Z_{eff} = \frac{\sum_i f_i A_i \left(\frac{\mu}{\rho}\right)_i}{\sum_j f_j \frac{A_j}{Z_j} \left(\frac{\mu}{\rho}\right)_j} \quad (5)$$

where A_i and Z_i represent the atomic weight and atomic number for ith element, respectively, and f_i denotes its fractional abundance concerning the number of atoms.

Effective electron density (N_{eff})

The N_{eff} of samples can be calculated using the following formula:

$$N_{eff} = N_A \frac{n Z_{eff}}{\sum_i n_i A_i} = N_A \frac{Z_{eff}}{A} \, (\text{electrons/g}) \quad (6)$$

where N_A = Avogadro's number (6.022×10^{23}/mol), $<A>$ = sample's average atomic mass,

Z_{eff} = effective atomic number, and A_i and n_i are the atomic mass and molar fraction of ith element in the sample, respectively.

Half-value layer (HVL) and tenth-value layer (TVL)

For shielding materials, HVL and TVL can be evaluated using 'μ' at specific gamma-ray energy from the following relations:

$$HVL = \frac{\ln(2)}{\mu} = \frac{0.693}{\mu} \; (cm) \tag{7}$$

and

$$TVL = \frac{\ln(10)}{\mu} = \frac{2.303}{\mu} \; (cm) \tag{8}$$

Mean free path (MFP)

The MFP of a material can be computed by the following equation:

$$MFP = \frac{1}{\mu} \; (cm) \tag{9}$$

where μ = linear attenuation coefficient at a particular photon energy

Total atomic cross-section (σ_a) and total electronic cross-section (σ_e)

The 'σ_a' for a material can be derived from the below formula:

$$\sigma_a = \frac{\mu/\rho}{N_A \sum_i \frac{w_i}{A_i}} \; (barn/atom) \tag{10}$$

where μ/ρ = mass attenuation coefficient, N_A = Avogadro's number, A_i = atomic weight, and w_i = weight fraction of each element present in the material.

The 'σ_e' can be computed by the following equation:

$$\sigma_e = \frac{1}{N_A} \sum_i \frac{f_i A_i}{Z_i} \left(\frac{\mu}{\rho}\right)_i \; (barn/electron) \tag{11}$$

where f_i = fractional abundance of element 'i', Z_i = atomic number of ith element.

Here, the ratio between (σ_a) and (σ_e) represents Z_{eff} as given below:

$$Z_{eff} = \frac{\sigma_a}{\sigma_e} \tag{12}$$

Results and discussion

Gamma-ray attenuation features

Figure 2a, b shows the comparison of the μ/ρ values for all selected S1–S5 and P1–P6 samples calculated using WinXCom and MCNP5 code within the 0.015–15 MeV photon energy range, respectively. For all samples, one can notice a good match between μ/ρ values derived from the WinXCom program and MCNP5 code (Fig. 2). In Table 3 (i) and (ii), we have presented the evaluated μ/ρ values using WinXCom and MCNP5 code for all the S1–S5 and P1–P6 glasses, respectively, along with % deviation [computed using Eq. (1)] between them. As shown in Table 3 data, the calculated deviation values between WinXCom and MCNP5 results are varied within the range of 0.01734–7.10324%, 0.05525–7.1463%, 0.05928–7.14414%, 0.06792–7.17188%, and 0.07694–7.19647% for S1, S2, S3, S4, and S5 samples, while for P1, P2, P3, P4, P5, and P6 glasses they are in the 0.05001–7.01486%, 0.07272–7.05429%, 0.06528–7.21135%, 0.07204–7.31472%, 0.07423–7.44494%, and 0.07428–7.47487% fluctuating range, overall with < 7.5% deviation. From Fig. 2, it is identified that μ/ρ values decrease with increasing γ-ray energy and increase with Bi_2O_3 content increment in the S1–S5 and P1–P6 glasses. The WinXCom μ/ρ values increase from 49.39 to 62.47 cm^2/g, and 45.58 to 76.48 cm^2/g at 15 keV for S1 → S5 and P1 → P6 samples, respectively, where sample P6 possesses the highest μ/ρ value, suggesting it has a better absorber. Among all the selected glasses, due to the lowest density, the P1 sample shows the least photon attenuation ability. This one suggests that higher photon interactions will occur for higher Bi_2O_3 (i.e., high Z element) content-added samples and also at lower photon energies (0.015–0.04 MeV, PE absorption dominance). This implies that with an increase in incident photon energy, there occurs a decrease in the attenuation, leading to enhanced penetration of γ-rays in the glass. Further, μ/ρ values for all samples decrease quickly with an increment in the photon energy up to 0.8 MeV (PE effect influence), and then, they are almost constant (independent of photon energy) within the 1–4 MeV energy range where the CS process dominates. Afterward, μ/ρ values increase slightly which could be due to the PP process (nuclear and electric). Here, the dependence of cross-sections for PE, CS, and PP

Figure 2 Comparison of the WinXCom and MCNP5 calculated values of mass attenuation coefficients (μ/ρ, cm^2/g) versus photon energy for all **a** S1–S5 and **b** P1–P6 glasses.
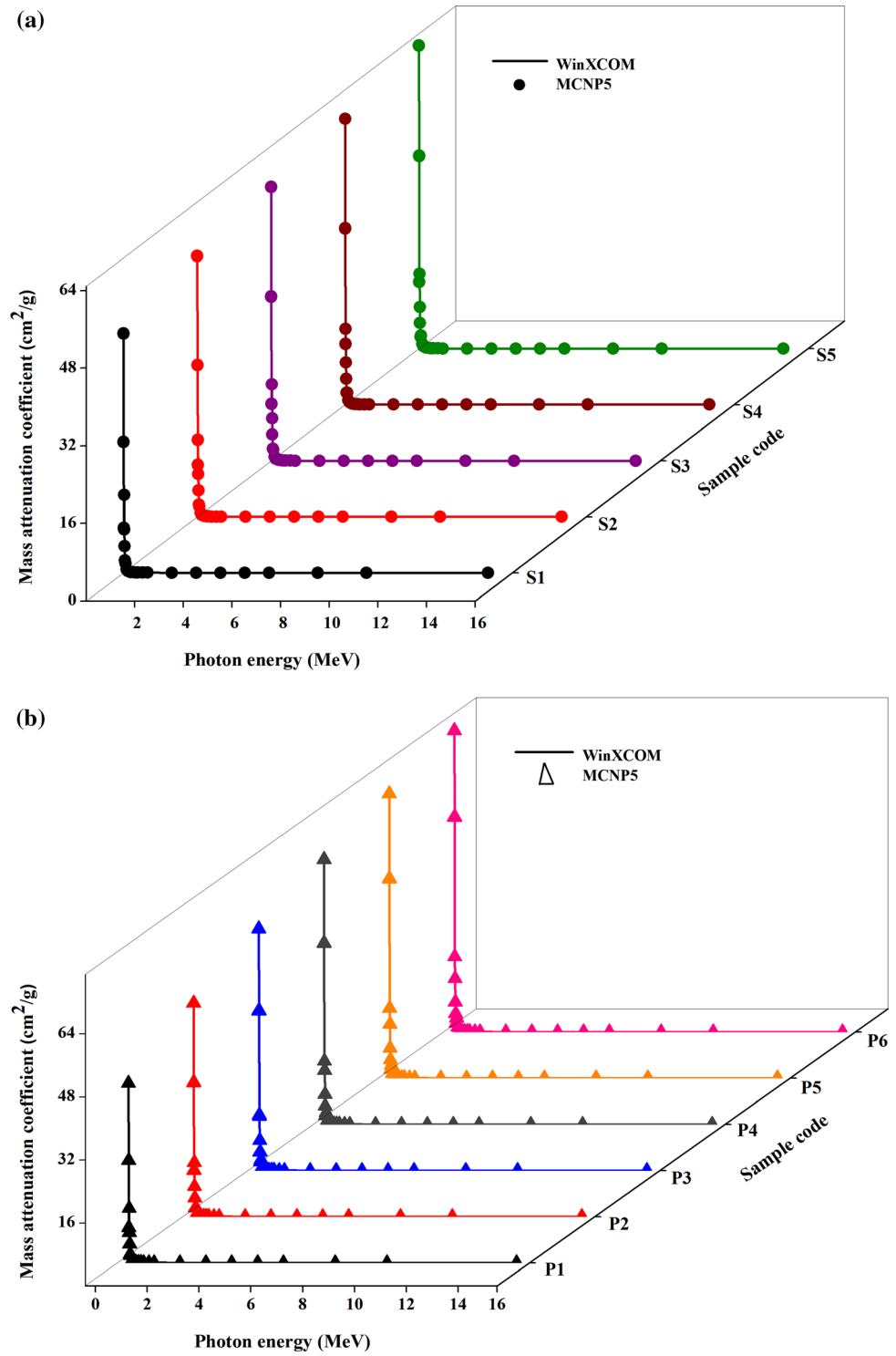
processes on photon energy is $E^{-3.5}$, E^{-1}, and log E, respectively [32]. In Fig. 2 (Table 3 data also), discontinuities are observed due to the PE effect near the K-absorption edges of 'Bi' and 'Te' elements at 100 keV and 40 keV energies, respectively, where B (0.188 keV) and O (0.532 keV) elements have low

K-edge x-ray absorption and do not add up much. The WinXCom's μ/ρ values are further considered for computation of associated shielding parameters.

Figure 3 shows the Z_{eff} variations within the photon energy range of 0.015–15 MeV for all (a) S1–S5 and (b) P1–P6 glasses. Here, Z_{eff} values are changed

Table 3 Mass attenuation coefficients (μ/ρ) of all (i) S1–S5 and (ii) P1–P6 glasses evaluated using WinXCom program and MCNP5 code, and % deviation

Energy (MeV)	S1			S2			S3		
	WinXCom	MCNP5	% deviation	WinXCom	MCNP5	% deviation	WinXCom	MCNP5	% deviation
(i) S1–S5 samples									
0.015	49.39	49.3526	0.07573	53.77	53.73127	0.07204	56.45	56.41653	0.05928
0.02	27.08	27.00207	0.28777	31.34	31.23789	0.32581	33.95	33.83503	0.33866
0.03	9.296	9.20136	1.01809	10.82	10.7283	0.84754	11.75	11.66252	0.74452
0.04	16.14	16.10996	0.18615	15.93	15.89447	0.22304	15.79	15.7616	0.17985
0.05	8.976	8.97147	0.05047	8.861	8.85392	0.07993	8.79	8.78204	0.0906
0.06	5.54	5.53904	0.01734	5.474	5.47098	0.05525	5.433	5.42862	0.08069
0.08	2.588	2.58024	0.29989	2.564	2.55242	0.45145	2.549	2.53544	0.53215
0.1	1.963	1.95857	0.22574	2.218	2.21215	0.26379	2.375	2.36775	0.30537
0.15	0.7244	0.71975	0.64132	0.8169	0.81194	0.60768	0.8736	0.86829	0.60734
0.2	0.3843	0.38037	1.02251	0.4286	0.42469	0.91148	0.4559	0.45163	0.93631
0.3	0.1861	0.1836	1.34539	0.202	0.19945	1.26462	0.2117	0.20934	1.11298
0.4	0.1271	0.12664	0.36058	0.1349	0.13379	0.82394	0.1397	0.13833	0.97776
0.5	0.1008	0.10233	1.51387	0.1053	0.10663	1.26528	0.1081	0.10918	0.99572
0.6	0.08598	0.08575	0.26536	0.08893	0.08856	0.41469	0.09073	0.08996	0.85273
0.8	0.06939	0.06859	1.15009	0.07091	0.06993	1.37593	0.07184	0.07074	1.52697
1	0.05985	0.05834	2.52864	0.06077	0.05915	2.67278	0.06133	0.05965	2.7321
2	0.04171	0.04105	1.57968	0.04208	0.04141	1.59938	0.04231	0.04163	1.60419
3	0.03685	0.03626	1.60836	0.03727	0.03666	1.63415	0.03752	0.0369	1.64145
4	0.0351	0.0346	1.41947	0.03559	0.03507	1.46164	0.03589	0.03535	1.50292
5	0.03456	0.03373	2.41151	0.03512	0.03425	2.47921	0.03547	0.03457	2.54386
6	0.03458	0.03399	1.69436	0.03521	0.03461	1.70244	0.03559	0.03499	1.69234
8	0.03541	0.03397	4.06673	0.03615	0.03468	4.06653	0.03661	0.03511	4.08677
10	0.03667	0.03407	7.10324	0.03752	0.03484	7.1463	0.03803	0.03531	7.14414
15	0.04007	0.04285	6.94306	0.04112	0.04398	6.95007	0.04176	0.04464	6.89379

Energy (MeV)	S4			S5		
	WinXCom	MCNP5	% deviation	WinXCom	MCNP5	% deviation
0.015	58.97	58.92994	0.06792	62.47	62.42194	0.07694
0.02	36.4	36.27022	0.35653	39.8	39.65625	0.36119
0.03	12.62	12.5404	0.63078	13.83	13.75692	0.52845
0.04	15.67	15.63781	0.20545	15.5	15.46389	0.23297
0.05	8.724	8.71491	0.10417	8.633	8.62077	0.14165
0.06	5.395	5.38909	0.10956	5.343	5.33497	0.1502
0.08	2.534	2.51919	0.58437	2.515	2.49705	0.71366
0.1	2.522	2.51351	0.33646	2.726	2.71709	0.32703
0.15	0.9268	0.92132	0.59174	1.001	0.9946	0.63895
0.2	0.4814	0.47716	0.87984	0.5168	0.51267	0.7985
0.3	0.2208	0.21852	1.0312	0.2335	0.23048	1.29224
0.4	0.1441	0.1427	0.9746	0.1503	0.1487	1.06486
0.5	0.1107	0.11174	0.94381	0.1143	0.11529	0.86963
0.6	0.09242	0.0915	0.99162	0.09477	0.09426	0.54103
0.8	0.07271	0.0718	1.25213	0.07392	0.07323	0.93232
1	0.06185	0.0601	2.83673	0.06258	0.06074	2.93781
2	0.04253	0.04186	1.56854	0.04282	0.0421	1.68094
3	0.03776	0.03712	1.70448	0.0381	0.03747	1.64286
4	0.03617	0.03562	1.51424	0.03656	0.03599	1.55885
5	0.03579	0.03487	2.5799	0.03624	0.03529	2.63204

Table 3 continued

Energy (MeV)	S4			S5		
	WinXCom	MCNP5	% deviation	WinXCom	MCNP5	% deviation
6	0.03595	0.03534	1.68766	0.03645	0.03584	1.68515
8	0.03704	0.03552	4.09204	0.03763	0.03609	4.08329
10	0.03852	0.03576	7.17188	0.03919	0.03637	7.19647
15	0.04237	0.04529	6.88634	0.04321	0.04615	6.81381

Energy (MeV)	P1			P2			P3		
	WinXCom	MCNP5	% deviation	WinXCom	MCNP5	% deviation	WinXCom	MCNP5	% deviation
(ii) P1–P6 samples									
0.015	45.58	45.54776	0.07074	54.24	54.20056	0.07272	61.32	61.27997	0.06528
0.02	26.07	25.99792	0.27648	34.1	33.98082	0.3495	40.66	40.50527	0.38055
0.03	8.994	8.91878	0.83637	11.85	11.78055	0.58606	14.18	14.12157	0.41206
0.04	13.9	13.87294	0.19467	13.83	13.80274	0.19709	13.78	13.74883	0.22618
0.05	7.742	7.73812	0.05006	7.712	7.70505	0.09012	7.687	7.67521	0.15344
0.06	4.789	4.7866	0.05001	4.778	4.77077	0.15136	4.769	4.75626	0.26722
0.08	2.251	2.24052	0.46544	2.255	2.24051	0.64243	2.259	2.23942	0.86684
0.1	1.872	1.86382	0.437	2.358	2.34894	0.38441	2.755	2.74503	0.3618
0.15	0.6999	0.69479	0.73016	0.8746	0.86901	0.63942	1.017	1.01108	0.5825
0.2	0.3752	0.37112	1.08686	0.4586	0.4535	1.11114	0.5268	0.52234	0.84692
0.3	0.1846	0.1823	1.24538	0.2141	0.21193	1.01407	0.2383	0.23551	1.17004
0.4	0.1272	0.12748	0.22112	0.1416	0.14097	0.44489	0.1533	0.15193	0.8913
0.5	0.1014	0.1042	2.76511	0.1097	0.11153	1.66932	0.1165	0.11791	1.20942
0.6	0.08675	0.08698	0.2604	0.09208	0.0915	0.63039	0.09644	0.09568	0.78864
0.8	0.07026	0.06901	1.78269	0.07293	0.07214	1.08622	0.07512	0.07408	1.39105
1	0.0607	0.0592	2.46993	0.06227	0.06055	2.7567	0.06354	0.06165	2.9702
2	0.04217	0.04153	1.52006	0.04279	0.04205	1.72162	0.0433	0.04256	1.70528
3	0.03685	0.03629	1.51138	0.03762	0.03704	1.52883	0.03825	0.03756	1.81343
4	0.03472	0.03423	1.39891	0.03568	0.03515	1.48391	0.03647	0.03591	1.53719
5	0.03386	0.03308	2.31112	0.03501	0.03413	2.50346	0.03594	0.03501	2.59291
6	0.03362	0.03305	1.68959	0.03492	0.03433	1.68776	0.03598	0.03537	1.69565
8	0.03402	0.03266	3.98327	0.0356	0.03417	4.0258	0.03689	0.03538	4.10517
10	0.03493	0.03251	6.92858	0.03675	0.03416	7.05429	0.03824	0.03548	7.21135
15	0.03768	0.04032	7.01486	0.03998	0.04271	6.83036	0.04186	0.04458	6.48882

Energy (MeV)	P4			P5			P6		
	WinXCom	MCNP5	% deviation	WinXCom	MCNP5	% deviation	WinXCom	MCNP5	% deviation
0.015	67.22	67.17157	0.07204	72.21	72.1564	0.07423	76.48	76.42319	0.07428
0.02	46.12	45.94425	0.38108	50.74	50.54249	0.38926	54.7	54.48604	0.39114
0.03	16.12	16.06849	0.31954	17.77	17.71829	0.291	19.18	19.13197	0.2504
0.04	13.73	13.70254	0.19998	13.69	13.66218	0.20321	13.66	13.62803	0.23406
0.05	7.666	7.65182	0.18492	7.649	7.63099	0.2355	7.634	7.61368	0.26623
0.06	4.761	4.74592	0.31682	4.755	4.73682	0.38231	4.749	4.72822	0.43764
0.08	2.262	2.23889	1.02163	2.264	2.23839	1.13114	2.266	2.23793	1.23858
0.1	3.087	3.07454	0.40368	3.366	3.35374	0.36421	3.606	3.59217	0.38362
0.15	1.136	1.12915	0.60288	1.237	1.22894	0.65158	1.323	1.31443	0.6481
0.2	0.5836	0.57896	0.79537	0.6316	0.62688	0.74668	0.6727	0.66785	0.7213
0.3	0.2584	0.25546	1.1375	0.2754	0.27242	1.08336	0.29	0.28676	1.11581
0.4	0.1631	0.16109	1.23284	0.1713	0.16952	1.04162	0.1784	0.17636	1.14316

Table 3 continued

Energy (MeV)	P4			P5			P6		
	WinXCom	MCNP5	% deviation	WinXCom	MCNP5	% deviation	WinXCom	MCNP5	% deviation
0.5	0.1221	0.12291	0.6671	0.1269	0.1272	0.23418	0.131	0.13102	0.01784
0.6	0.1001	0.09924	0.86058	0.1031	0.1025	0.5825	0.1058	0.10479	0.95903
0.8	0.07694	0.07558	1.76993	0.07848	0.07727	1.5359	0.0798	0.07857	1.54315
1	0.06461	0.06259	3.12062	0.0655	0.06336	3.26343	0.06627	0.06406	3.3415
2	0.04372	0.04295	1.77004	0.04408	0.04326	1.86128	0.04439	0.04356	1.87341
3	0.03878	0.03809	1.78428	0.03923	0.03853	1.78612	0.03961	0.03886	1.88316
4	0.03713	0.03652	1.65394	0.03768	0.03705	1.67345	0.03816	0.03749	1.74596
5	0.03671	0.03572	2.69176	0.03737	0.03633	2.78077	0.03793	0.03686	2.82486
6	0.03687	0.03623	1.72614	0.03762	0.03696	1.74343	0.03826	0.0376	1.72508
8	0.03797	0.03639	4.16582	0.03888	0.03724	4.22214	0.03966	0.03798	4.23289
10	0.03947	0.03658	7.31472	0.04052	0.0375	7.44494	0.04141	0.03831	7.47487
15	0.04343	0.04612	6.19387	0.04475	0.04739	5.90944	0.04588	0.04858	5.87575

both with the photon energy and the Bi_2O_3 content addition (composition of the glass), and from Fig. 3, one can identify that, initially, for all samples, the values of Z_{eff} are the maximum in the low energy region (0.015–0.03 MeV) due to PE absorption and then slightly decreased at the 0.04–0.08 MeV energy range. In consequence of the PE effect, a sudden jump was noticed at 0.1 MeV due to 'Bi' element K-absorption edge. In our study, two L-absorption edges for Bi element, i.e., L1 (16.39 keV) and L2 (15.71 keV), can also be observed within the selected photon energy range (0.015–15 MeV). Further, from 0.1 to 0.8 MeV, Z_{eff} values are decreased steeply with photon energy increment (PE effect control) and variation in Z_{eff} is negligible from 0.8 to 2 MeV due to CS process dominance, where the Z_{eff} reached the lowest values (at 1.5 MeV) in this energy interval. Beyond 2 MeV energy, one can see a slow increase in the Z_{eff} values with increasing photon energy up to 15 MeV because of the effect of PP at this higher energy region. Here, it should be noted that the Z-dependence of cross-sections for PE absorption, CS, and PP processes is Z^{4-5}, Z, and Z^2, respectively. Moreover, with Bi_2O_3 content increment in the S1–S5 and P1–P6 samples, an increase in the Z_{eff} values was noticed (Fig. 3). The increase in Z_{eff} value by the inclusion of a higher amount of Bi_2O_3 from S1 → S5 and P1 → P6 samples is due to the increase in the mole fraction and/or weight fraction of higher Z constituent, Bi ($Z = 83$) (Tables 1 and 2). Here, similarly to the μ/ρ results, the P6 sample possesses the highest Z_{eff} value (72.35) at 0.015 MeV among all

the selected glasses. Generally, for a glass to be used as an efficient γ-ray shield, it should have a large value of Z_{eff}, where photons are more likely to be absorbed by the available large number of electrons with higher interaction probability, so, sample P6 is a superior absorber compared with all other chosen glasses.

For all S1–S5 and P1–P6 samples, the dependences of the N_{eff} values with the photon energy in the range of 0.015–15 MeV are presented in Fig. 4a, b, respectively. The zoom-in N_{eff} variations at 7–15.5 MeV and 7.4–15.2 MeV photon energies for all S1–S5 and P1–P6 glasses are illustrated in the inset plots of Fig. 4a, b. Here, one can notice that the fluctuations in N_{eff} values are very similar to the trends identified for Z_{eff} values as the N_{eff} acquired from the Z_{eff} depends on the A(average atomic mass) also, where Z represents the number of protons or electrons in any sample. The N_{eff} quantities for all S1–S5 and P1–P6 glasses have an inversely identical change to the Z_{eff} within the 0.04–0.08 MeV photon energy. Moreover, the N_{eff} values are varied within the range of 5.94×10^{23}–6.16×10^{23} electrons/g for S1 → S5 samples at 0.015 MeV photon energy, while for P1 and P6 samples the N_{eff} values are 8.31×10^{23} and 7.53×10^{23} electrons/g, respectively. Further, samples S1 and P1 show the lowest N_{eff} values in their respective series glasses within the 0.1–15 MeV and 0.15–15 MeV photon energy range. Thus, Z_{eff} and N_{eff} quantities can be used for the optimization of the shielding features for materials.
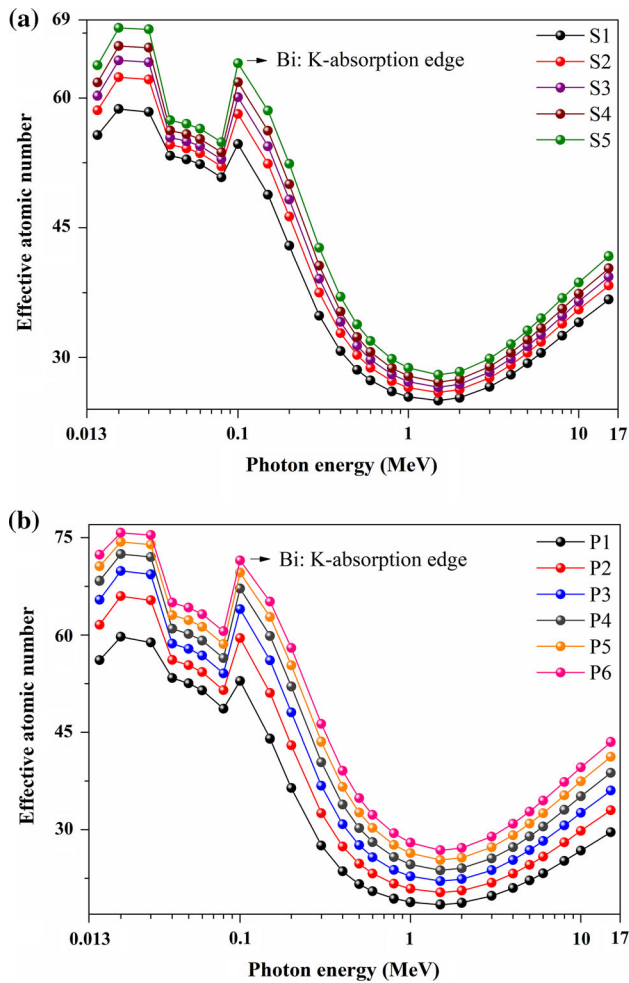
Figure 3 Variation of effective atomic number (Z_{eff}) with photon energy for all **a** S1–S5 and **b** P1–P6 glasses.
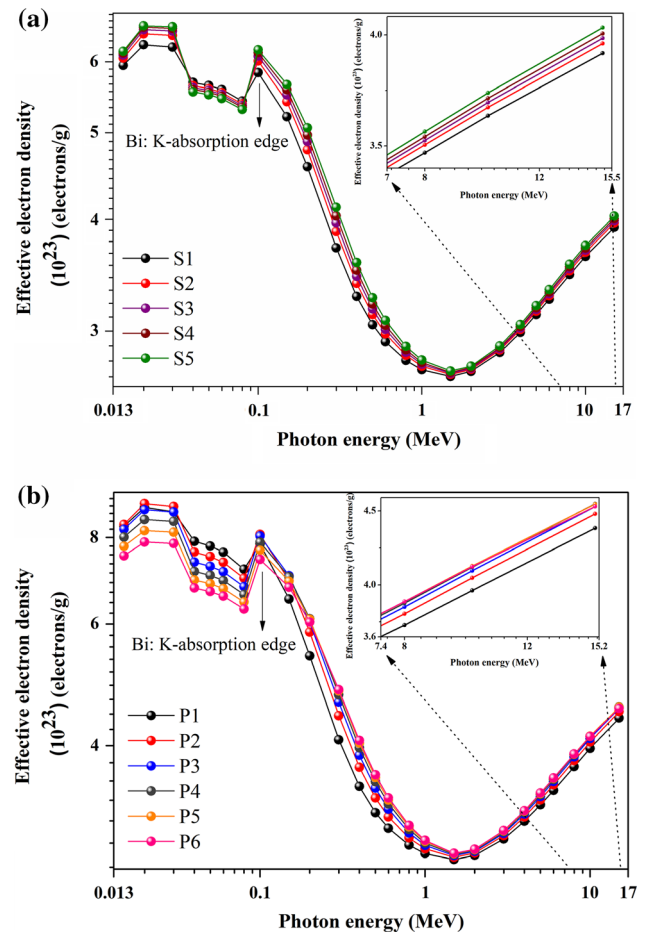

Figure 4 Variation of effective electron density (N_{eff}) with photon energy for all **a** S1–S5 (inset, within the range of 7–15.5 MeV photon energy) and **b** P1–P6 (inset, within the 7.4–15.2 MeV photon energy range) glasses.

The changes in HVL and TVL values derived within 0.015 MeV–10 MeV energy range for all S1–S6 and P1–P6 samples are shown in Figs. 5a, b, and 6a, b, respectively. The expanded energy regions at 0.05–0.16 MeV (S1–S5 glasses) and 0.04–0.2 MeV (P1–P6 samples) are given as inset plots of Figs. 5 and 6, respectively. From Figs. 5 and 6, one can see that for all selected samples, HVL and TVL values are very small at lower photon energies (≤ 0.15 MeV) and almost constant up to 0.1 MeV. Then, there occurs a quick increment in HVL and TVL values with increasing photon energy, reaching the highest value at 5 MeV for all S1–S5 samples. P1 and P2 glasses possess maximum HVL and TVL values at 6 MeV, while they are achieved at 5 MeV for all P3–P6 samples. From 6 and 8 MeV (for P1 and P2 samples) photon energy onward, one can notice that both HVL and TVL values show a minor reduction with

increasing energy up to 15 MeV. The identified HVL and TVL values at 5 MeV are 3.693 and 12. 269 cm, 3.468 and 11.521 cm, 3.341 and 11.098 cm, 3.212 and 10.669 cm, and 3.056 and 10.150 cm for S1, S2, S3, S4, and S5 glasses, respectively. Similarly, for P1 and P2 samples, 4.806 and 15.966 cm, and 4.127 and 13.709 cm at 6 MeV are the observed highest HVL and TVL values. At 5 MeV, the noticed maximum HVL and TVL values for P3, P4, P5, and P6 glasses are 3.709 and 12.321 cm, 3.396 and 11.280 cm, 3.170 and 10.532 cm, and 2.928 and 9.727 cm, respectively. The variations in HVL and TVL concerning photon energy can be interpreted as a consequence of PE absorption, CS, and PP processes in different energy regions the same as in the earlier μ/ρ and Z_{eff} values trend discussion. Further, HVL and TVL values decrease (reduction in the thickness) with increasing Bi$_2$O$_3$ content in all studied glasses. Generally, lower
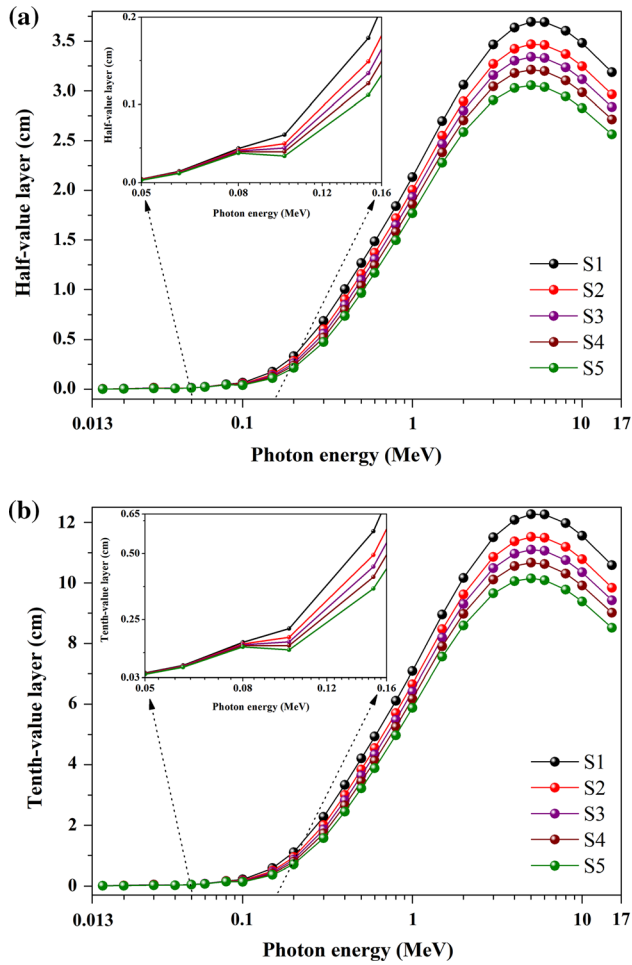
Figure 5 Variation of **a** half-value layer (HVL) (inset, within the 0.05–0.16 MeV photon energy range) and **b** tenth-value layer (TVL) (inset, within the range of 0.05–0.16 MeV photon energy) with photon energy for all S1–S5 glasses.
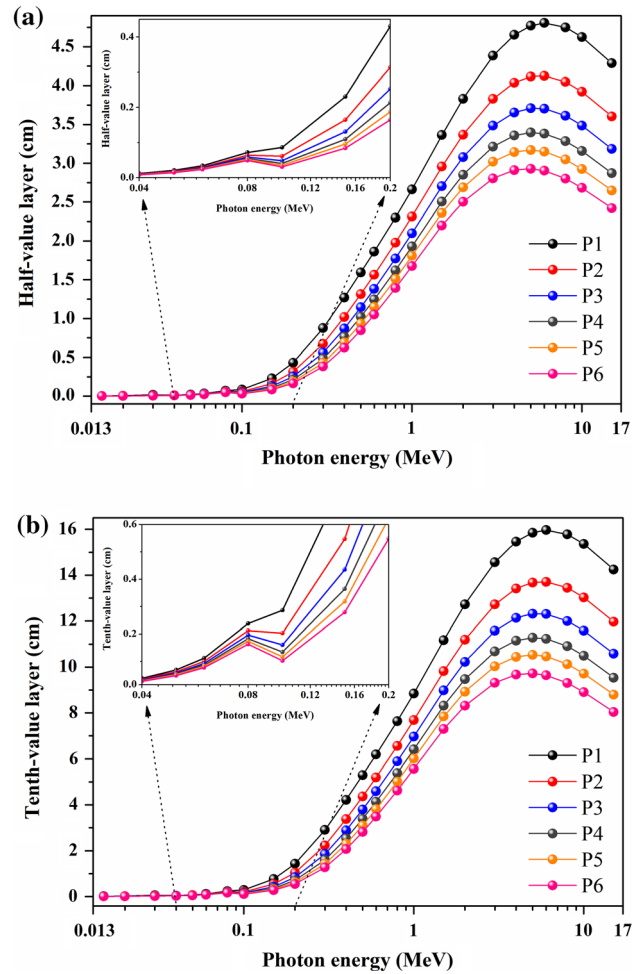

Figure 6 Variation of **a** half-value layer (HVL) (inset, within range of 0.04–0.2 MeV photon energy) and **b** tenth-value layer (TVL) (inset, within the 0.04–0.2 MeV photon energy range) with photon energy for all P1–P6 glasses.

HVL values are needed for a superior γ-ray shield, which causes more photon interactions with material (i.e., larger the density of the shield, higher the interactions of photons to lose their energy). Among all selected samples, glass P6 has the lowest HVL and TVL values within the 0.015–15 MeV energy range due to its higher density and μ/ρ values, indicating the P6 sample as a promising shield compared with other glasses. When space usability is a concern, all studied samples require lower thickness (reduced volume) for attenuating efficiently the low energy photons than that for higher energy ones where thicker glass is needed. From the γ-ray protection perspective, this means higher energy photons penetrate the sample more easily than the low energy photons.

The variation of MFP values within 0.015–15 MeV photon energy range for all S1–S5 and P1–P6 samples is presented in Fig. 7a, b, respectively, and inset plots show an enlarged energy region at the 0.05–0.2 MeV energy range. Here, one can observe that MFP values follow a similar trend as the HVL and TVL values for all the selected glasses. Up to ≤ 0.1 MeV energy, all the samples show very small MFP values; then, with an increase in energy the MFP values are also increased with a maximum value at 5 MeV for all S1–S5 samples, 6 MeV for P1 and P2 samples, and 5 MeV for all P3–P6 samples. After that, MFP values exhibit a decreasing trend up to 15 MeV for all samples. As explained for the above μ/ρ, Z_{eff}, HVL, and TVL values trend, here, for MFP values also, PE, CS, and PP processes play an important role in different (i.e., low, medium, and high) energy regions. At 5 MeV

photon energy, the identified MFP values for all S1–S5 samples are 5.328 cm, 5.004 cm, 4.820 cm, 4.634 cm, and 4.408 cm, respectively. For P1 and P2 samples, 6.934 cm and 5.954 cm are the maximum MFP values at 6 MeV energy, while at 5 MeV photon energy, P3–P6 samples possess 5.351 cm, 4.899 cm, 4.574 cm, and 4.225 cm values of MFP. From Fig. 7, it is observed that within the considered photon energy range, the MFP values are the lowest for S5 and P6 samples and are highest for S1 and P1 samples in their respective series and further P6 glass shows slightly lower values of MFP than that of S5 sample within the 0.015–15 MeV energy range. This implies that sample P6, having the highest Z_{eff}, is the best shielding glass among all selected samples as it is well known that the lower the MFP value, the better
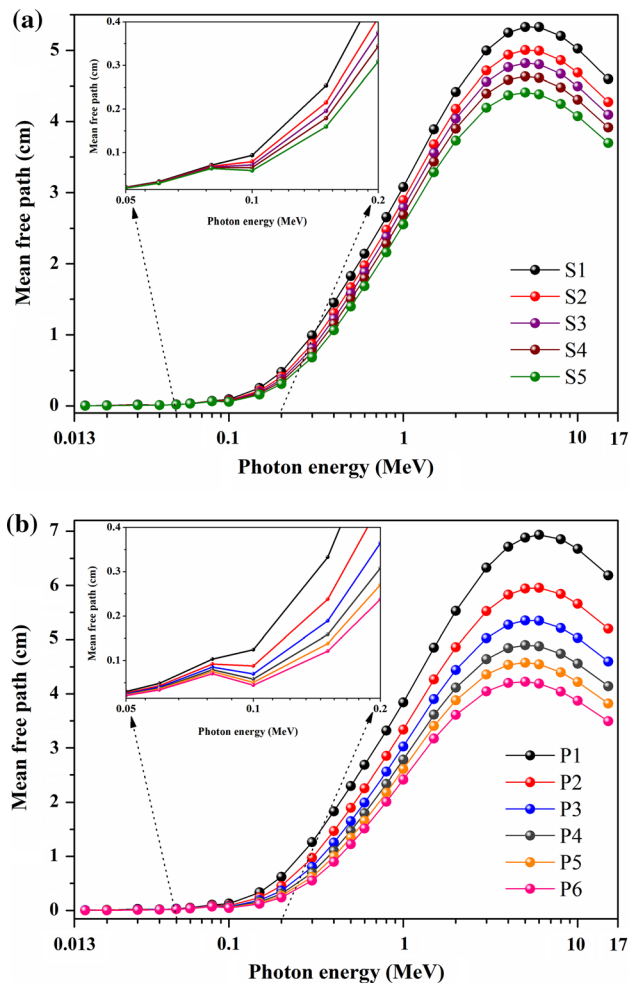
Figure 7 Variation of mean free path (MFP) with photon energy for all **a** S1–S5 (inset, within the 0.05–0.2 MeV photon energy range) and **b** P1–P6 (inset, within the range of 0.05–0.2 MeV photon energy) glasses.

the γ-ray attenuation (higher probability for photon interactions).

For all S1–S5 and P1–P6 samples, the changes in 'σ_a' (ACS) and 'σ_e' (ECS) values within the photon energy range of 0.015–15 MeV are depicted in Figs. 8a, b, and 9a, b, respectively. The respective zoom-in photon energy regions of 2–16 MeV, 1–16 MeV, and 5–15.5 MeV are shown as inset plots for Figs. 8a, b, and 9. Generally, for inorganic and organic materials, atomic, electronic, and molecular cross-sections can be measured in barn units (1 barn = 10^{-24} cm^2). For all selected samples, one can notice that both 'σ_a' and 'σ_e' values increase with high Z element (Bi) increment at lower photon energies, while the changes in these values are minimal at higher energies. Moreover, at 0.04 MeV energy, all S1–S5 samples show a slight increase in 'σ_a' and 'σ_e' values (Figs. 8a, 9a), and for P1–P6 glasses, only P1 and P2 samples have a slight increment in 'σ_a' value at 0.04 MeV energy, whereas all P3–P6 samples show a decrement for 'σ_a' value (Fig. 9a). Further, P1, P2, and P3 samples exhibit a slight increase in 'σ_e' value at 0.04 MeV photon energy, while sample P4 possesses almost the same value as 0.03 MeV energy and for P5 and P6 glasses, 'σ_e' value decreases (Fig. 9b). At low photon energies about $\sim$ 40 keV, mainly PE effect dominates due to electrons' presence in the samples, where the effects from nuclei are disordered only with various binding energies (BE) of electrons, as high Z materials impart higher BE for inner electrons. Usually, inorganic compounds such as HMO-based glasses possess larger Z_{eff}, while organic materials exhibit a smaller Z_{eff} ($\leq$ 10) [33].

The variations of EBF and EABF values within 0.015–15 MeV photon energy range as a function of 1, 5, 10, 20, 30, and 40 mfp (different penetration depths) for all S1–S5 and P1–P6 samples are shown in Figs. 10a–e, f–k and 11a–e, f–k, respectively. The related formulae and description of coefficients such as Z_{eq}, ((μ_m)$_{Compton}$/(μ_m)$_{Total}$) ratio (R), and G–P parameters fitting method details for EBF and EABF calculations can be found elsewhere [2, 6, 14, 25, 31]. As shown in Figs. 10 and 11, clearly, the smallest values of EBF and EABF were observed at the low photon energies ($\leq$ 0.1 MeV) due to PE absorption process, where abrupt peaks at 0.02 MeV and 0.04 MeV energies related to L1-absorption edge of Bi and K-absorption edge of Te elements are also identified which possess the highest Z among the constituents of the selected samples. Interestingly, one
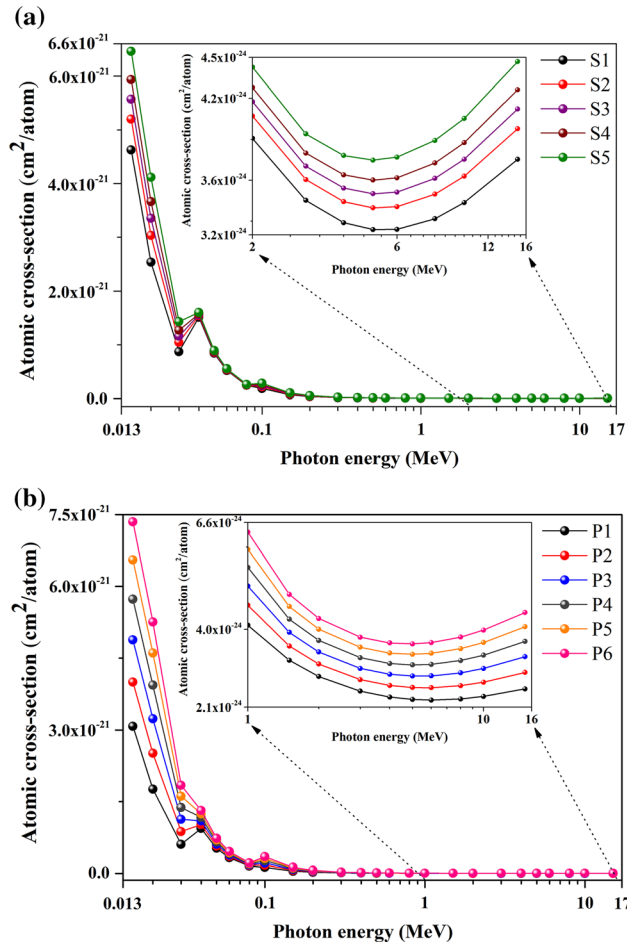
Figure 8 Variation of total atomic cross-section (ACS) with photon energy for all **a** S1–S5 (inset, within the 2–16 MeV photon energy range) and **b** P1–P6 (inset, within the range of 1–16 MeV photon energy) glasses.
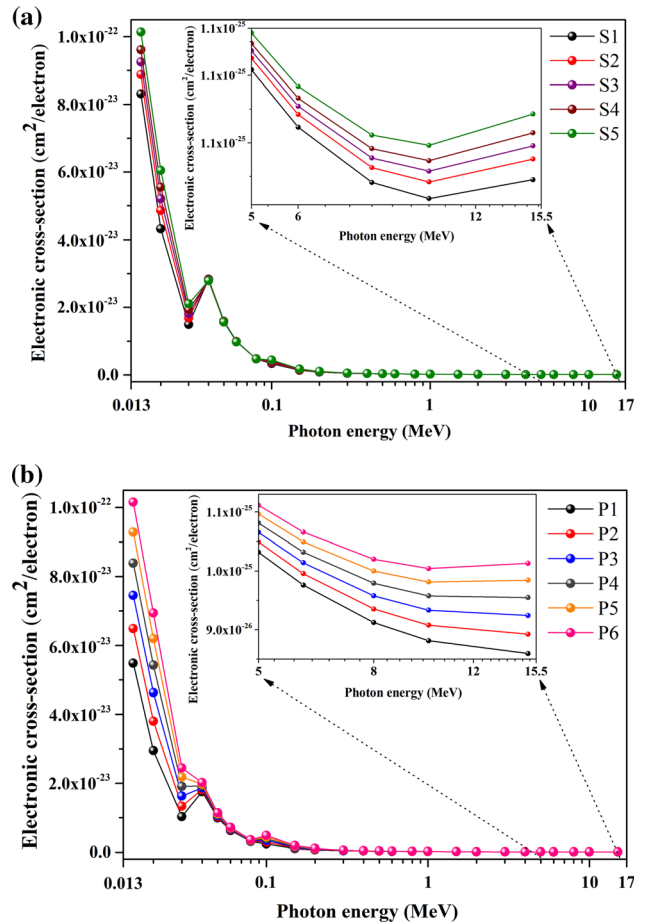
Figure 9 Variation of total electronic cross-section (ECS) with photon energy for all **a** S1–S5 (inset, within the range of 5–15.5 MeV photon energy) and **b** P1–P6 (inset, within the 5–15.5 MeV photon energy range) glasses.

can notice that the L1-absorption edge of 'Bi' becomes prominent than the K-absorption edge of 'Te' in all samples with progressive addition of Bi_2O_3 in place of TeO_2. With increasing photon energy, there occurs a slight gradual increase in the EBF and EABF values due to the CS process (multiple scattering processes) up to 5 MeV. Though EBF and EABF values usually relay on the sample chemical composition, at the CS process dominating region, chemical composition does not influence these values. Then, with a further increase in the photon energy, one can observe that for the penetration depths greater than 10 mfp, the EBF and EABF values have a noticeable increase in them due to the PP process. Such an increase could be due to a higher number of secondary photons, which raise very quickly as the penetration depth increases. Thus, PE and PP processes cause higher EBF and

EABF values at lower and higher photon energy regions, respectively. Moreover, it is found that the EBF and EABF values of all samples increase with increasing penetration depths at a certain photon energy. This behavior is due to the fact that the probability of the photon absorption process is higher when the photon goes deeper into the interacting medium. From Figs. 10 and 11, it is obvious that the EBF and EABF values decrease by the substitution of TeO_2 with Bi_2O_3 content in the glasses. The reason for this is that the molar mass of Bi_2O_3 (465.96 g/mol) is higher than that of TeO_2 (159.6 g/mol) molar weight. Such substitution leads to an increase in the density of the sample, causing higher Z_{eq}, and in turn reduction in EBF and EABF values. Generally, lower EBF and EABF values are required for samples to be used as better γ-ray attenuators. Consequently, S1
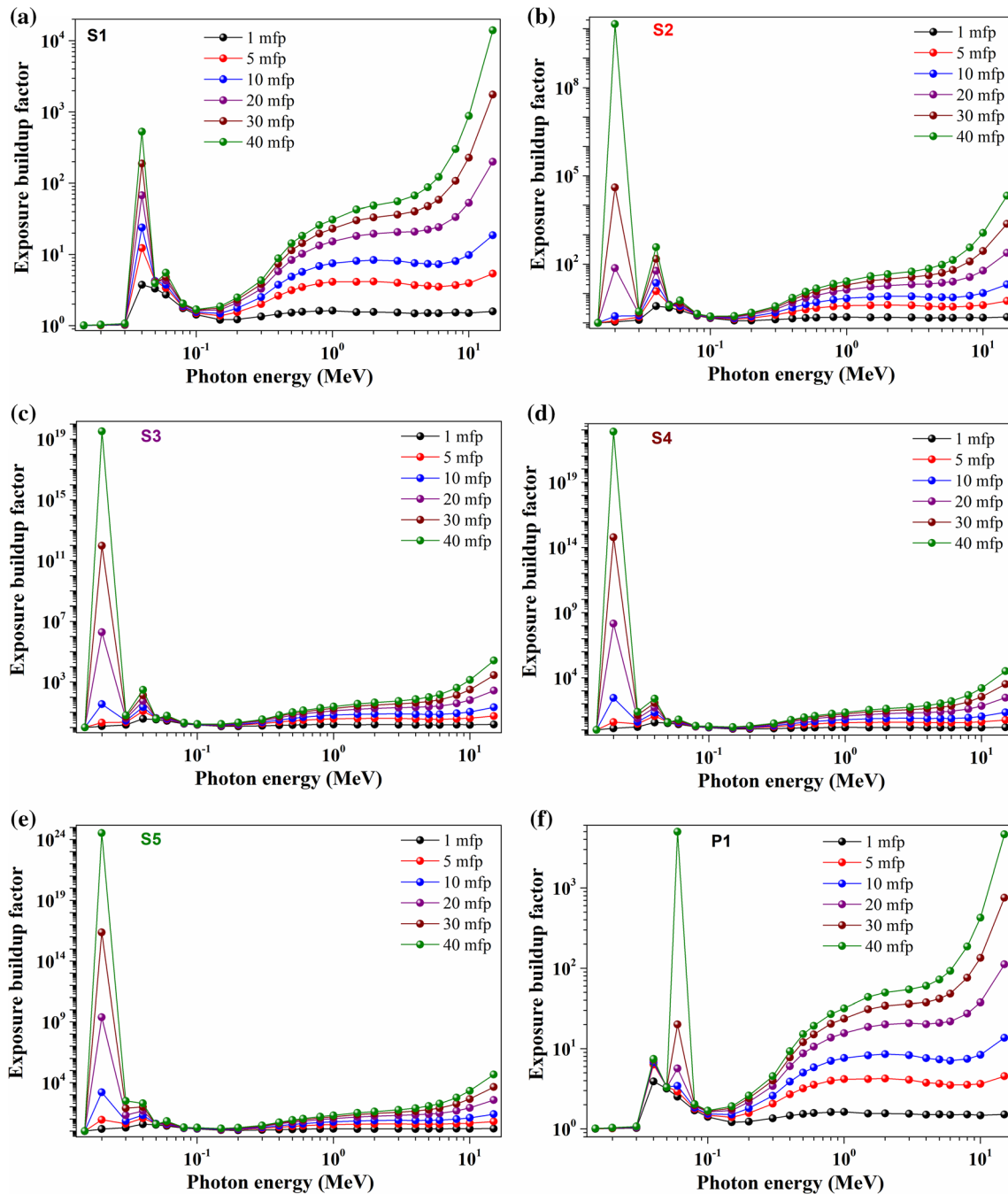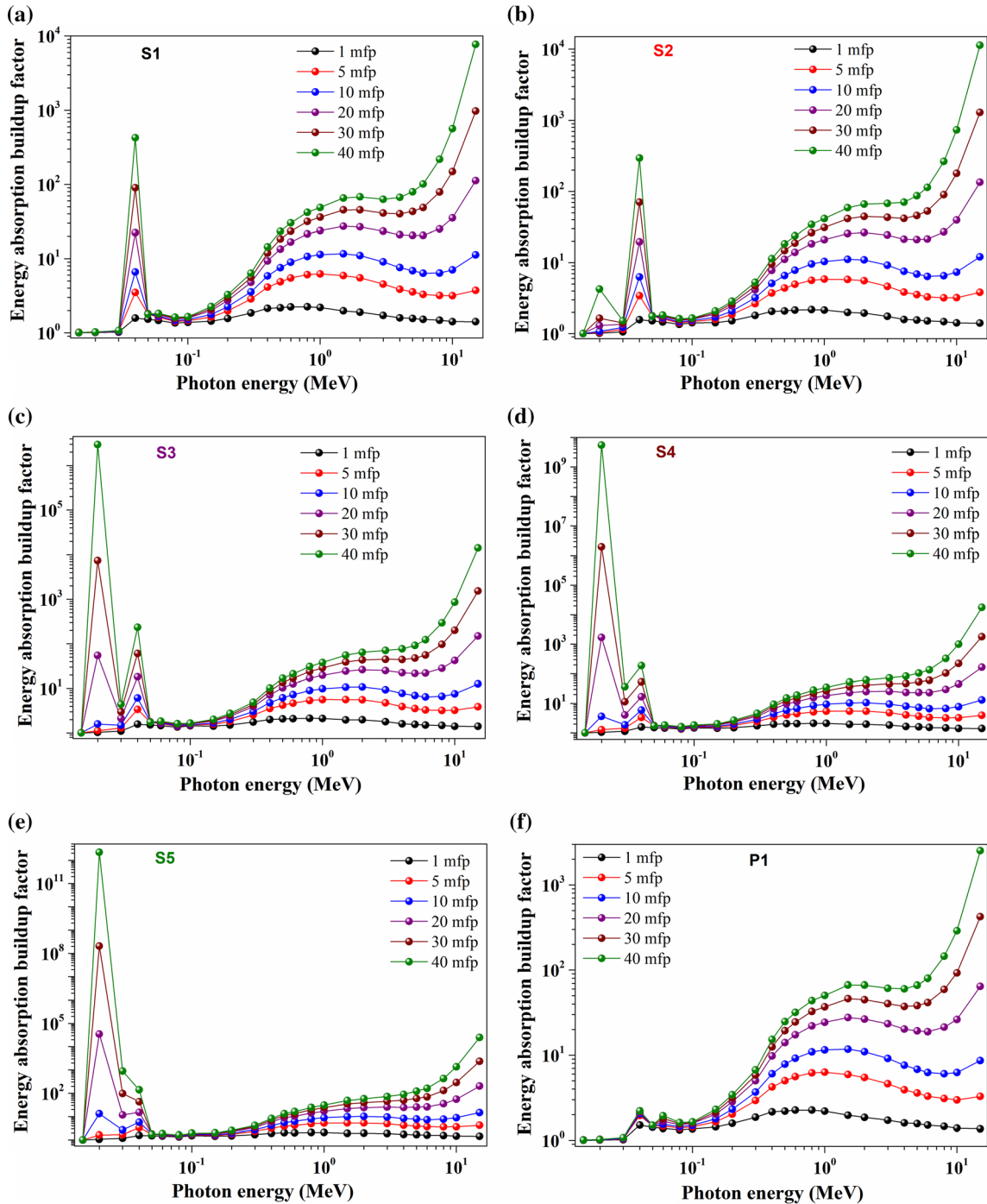
Figure 10 Variation of exposure buildup factor (EBF) with photon energy at different mean free paths for all **a–e** S1–S5 and **f–k** P1–P6 glasses.

and P1 glasses are found to possess the highest EBF and EABF values, while the lowest EBF and EABF values are observed for the S5 and P6 samples which could be suggested as excellent shields against γ-rays among all selected glasses.

To validate our EBF and/or EABF results, as an example, we have further evaluated the EBF values of H_2O through the G–P fitting parameter method and the obtained values are compared with that of standard ANSI/ANS-6.4.3 data [34]. Figure 12 presents such a comparison of EBF values of H_2O at different
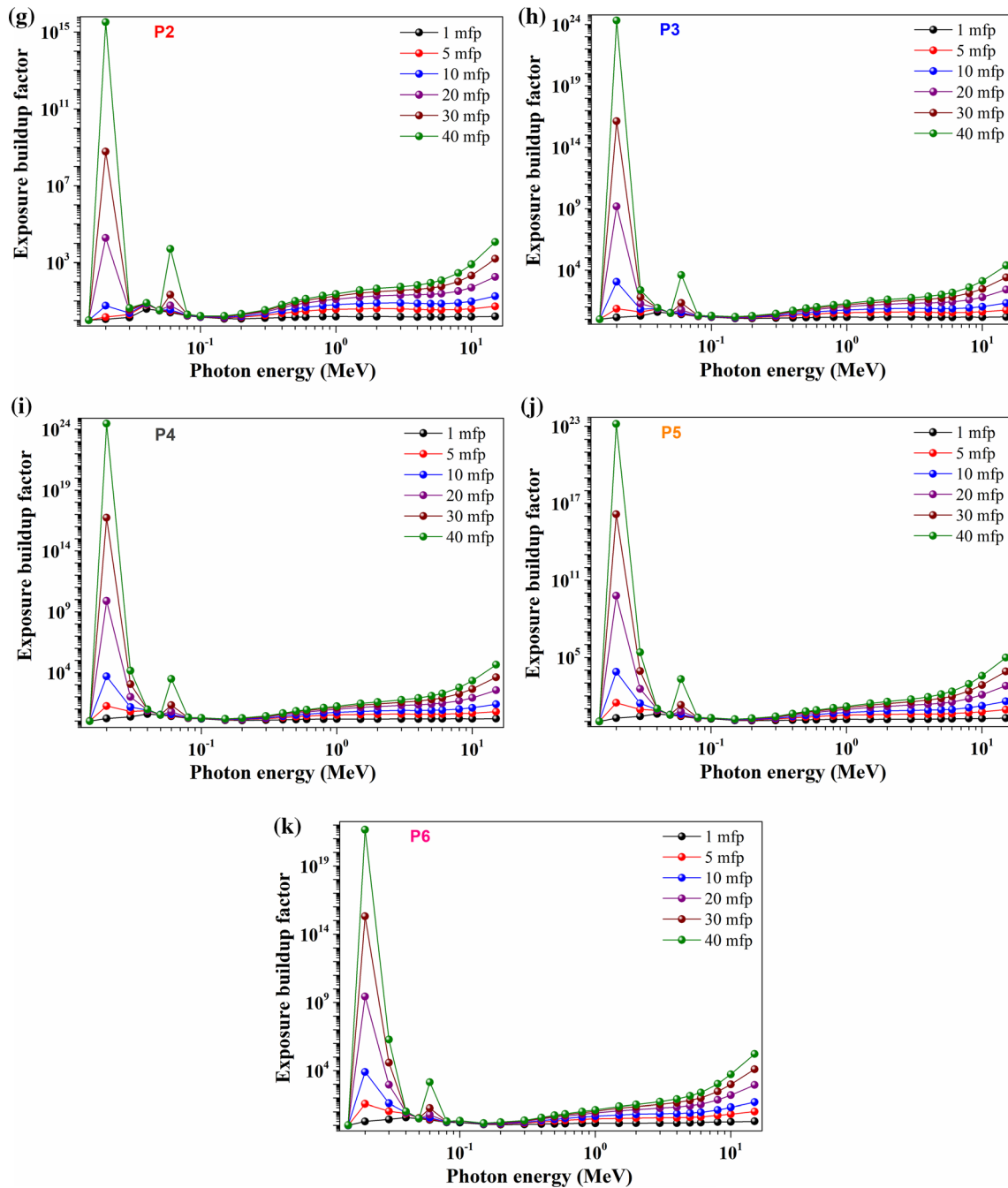
Figure 10 continued.

penetration depths of 5, 15, 25, and 35 mfp within the 0.015–15 MeV photon energy range. Here, one can clearly notice that the derived EBF values of H_2O by using the present method are fairly in agreement with conventional ANSI/ANS-6.4.3 data, indicating that uncertainties in γ-ray EBF or EABF values in the present work are insignificant.

Macroscopic effective removal cross-sections for fast neutrons ($\sum_R$)

The chances of a fast or fission energy neutron going through a particular reaction per unit path length of travel through any shielding material are measured as the macroscopic effective removal cross-sections (Σ_R), and Σ_R is almost constant within the 2–12 MeV neutron energy range. Elastic scattering is the only

Figure 11 Variation of energy absorption buildup factor (EABF) with photon energy at different mean free paths for all **a–e** S1–S5 and **f–k** P1–P6 glasses.

removal process for fast neutrons when the inelastic scattering becomes impossible at energies below the first excited state of any nucleus in the material. For various elements present in uniform mixtures, alloys, and composites, $(\sum_R)$ values can be evaluated using the following expression [24]:

$$\sum_R = \sum_i \rho_i \left(\sum_R / \rho \right)_i \tag{13}$$

where $'\rho_i'$ = partial density (g/cm^3) and $'\sum_{R/\rho}'$ (cm^2/ g) = mass removal cross-section of ith constituent.
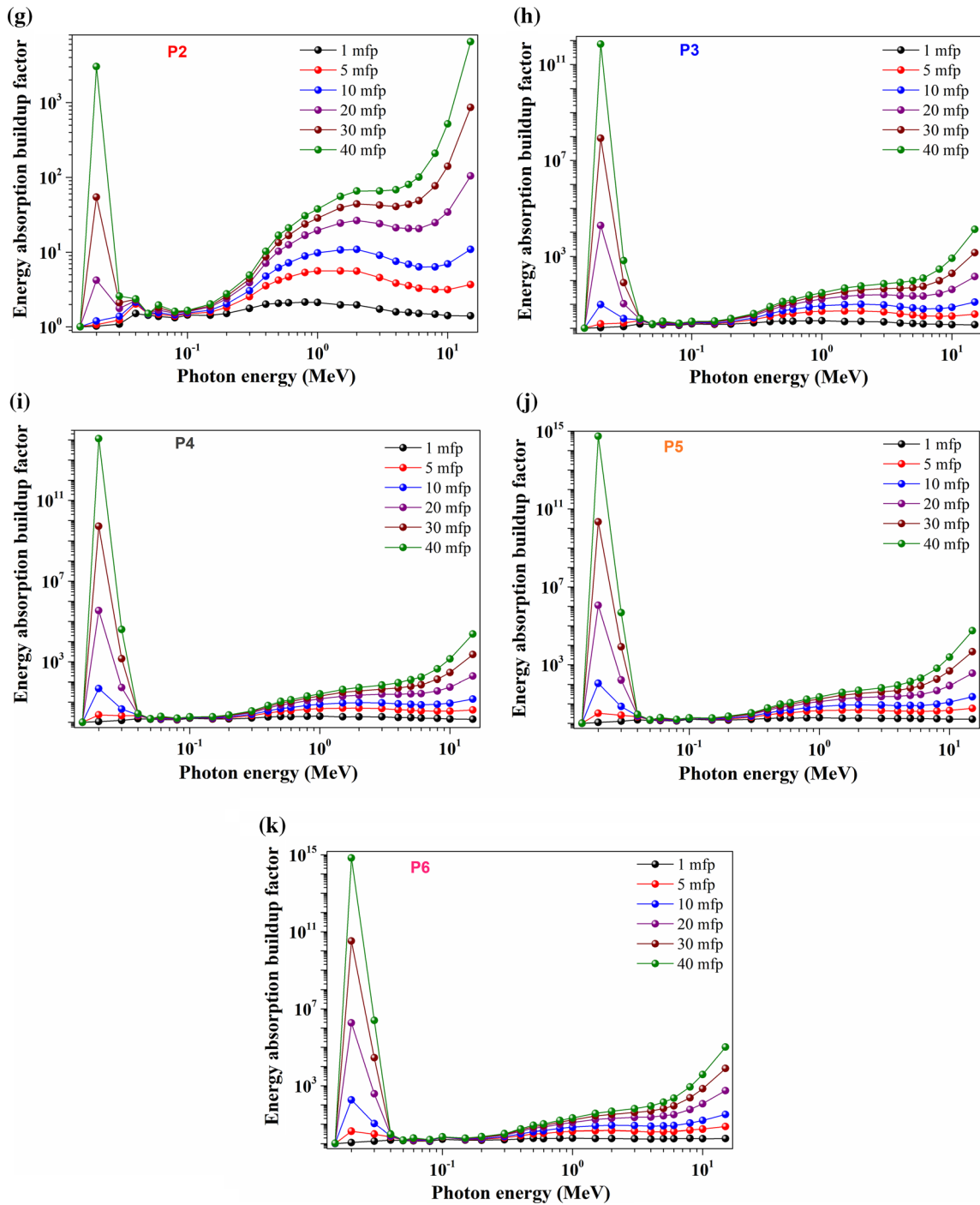
Figure 11 continued.

Table 4 presents the computed Σ_R values using Eq. (13) for all (i) S1–S5 and (ii) P1–P6 samples, respectively. From this table, one can notice that the values of Σ_R for S1–S5 and P1–P6 glasses are close among themselves with a slight increment following the Bi$_2$O$_3$ content, and varied within the range of 0.098–0.106 cm^{-1} and 0.093–0.108 cm^{-1}, respectively.

For S1–S5 samples, wt% of 'Bi' element increases at the expense of 'Te' and 'O' elements, while in P1–P6 glasses, wt% of 'Te,' 'B,' and 'O' elements decreased with an increase in 'Bi' element wt%. In glasses, although the presence of low Z elements (e.g., B) contributes to better neutron removal cross-section, a combination of both low and high Z elements (e.g.,
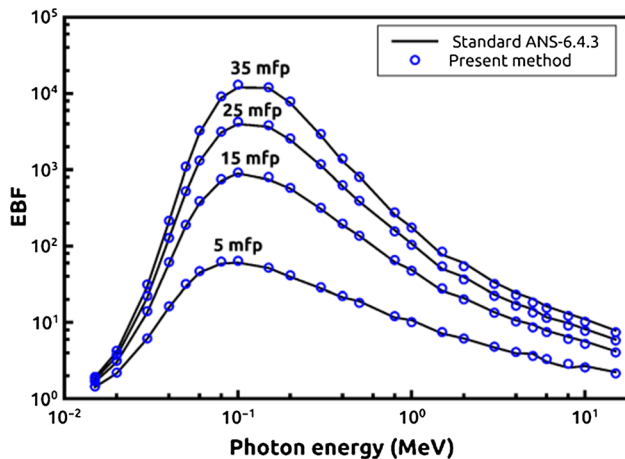
Figure 12 Comparison of EBF values of H_2O at 5, 15, 25 and 35 mfp derived using the present method and ANS-6.4.3 reference database.

Table 4 Effective removal cross-sections for fast neutrons Σ_R (cm^{-1}) for all (i) S1–S5 and (ii) P1–P6 glasses

Glass code	Σ_R
(i) S1–S5 samples	
S1	0.098
S2	0.101
S3	0.102
S4	0.104
S5	0.106
(ii) P1–P6 glasses	
P1	0.093
P2	0.098
P3	0.101
P4	0.103
P5	0.104
P6	0.108

Te, Bi) may also produce the similar results. From Table 4, it is identified that sample P6, which possesses a high density (6.24 g/cm^3) with Te, B, Bi, and O elements, has a high value of Σ_R, while minimum Σ_R is observed for P1 sample that has the lowest density among all the studied glasses. Thus, for fast neutron attenuation, the density of the sample plays a key role. Among all selected glasses, as sample P6 has the largest value of Σ_R, it is highly suitable for fast neutron shielding. Moreover, in this work, the computed $\sum_R = 0.108$ cm^{-1} value for sample P6 is larger in comparison with ordinary concrete ($\sum_{R} = 0.094$ cm^{-1}) and hematite serpentine

($\sum_R = 0.097$ cm^{-1}) [35], 80TeO$_2$–20K$_2$O ($\sum_{R} = 0.0924$ cm^{-1}), 80TeO$_2$–20BaO ($\sum_R = 0.1018$ cm^{-1}), and 80TeO$_2$–20ZnO ($\sum_R = 0.1007$ cm^{-1}) glasses [36], and BPAB glass ($\sum_R = 0.099$ cm^{-1}), LPAB glass ($\sum_R = 0.1047$ cm^{-1}) [24] including all studied B1–B6 ($\sum_R = 0.105354$–0.092256 cm^{-1}) and S1–S6 ($\sum_{R} = 0.101026$–0.106269) glasses [29].

Thermal neutron attenuation

During fission reactions in power plants and research reactors, when a fast neutron collides with hydrogen, a large amount of energy will be lost by fast neutron as the mass of neutrons and hydrogen nuclei is practically identical, maximizing energy transfer. This neutron scattering phenomenon converts a fast neutron into low-energy, thermal neutron. The thermal neutrons possess the kinetic energy of about 0.0253 eV and are in thermal equilibrium with atoms at ambient temperature (300 K). A thermal neutron can be easily absorbed through collision with elements, which have high neutron absorption cross-section such as boron (B). As '^{10}B' has a cross-section (several orders of magnitude higher than hydrogen) for ambient temperature neutrons of 3837 barns, it exhibits good shielding performance against thermal neutrons.

The total cross-section (σ_T) measures the probability that the interaction of any type will occur when neutron interacts with a target nuclei. In our study, the total cross-section (σ_T) determining the attenuation of neutrons is expressed in the following relation:

$$(\sigma_T) = (\sigma_{cs}) + (\sigma_{ics}) + (\sigma_A) \qquad (14)$$

where σ_{cs} is the coherent scattering cross-section, σ_{ics} is the incoherent scattering cross-section and σ_A corresponds to absorption cross-section due to nuclear capture processes.

Table 5 shows the evaluated σ_{cs}, σ_{ics}, σ_A, and σ_T values using the formula reported in Ref. [37] for all (i) S1–S5 and (ii) P1–P6 samples, respectively. From Table 5 data, it can be identified that the σ_{cs} values slightly increase from S1 → S5 and P1 → P6 samples, while σ_{ics} values decrease at the same time. Also, the σ_{cs} values are larger in two orders of magnitude than σ_{ics} values for S1–S5 samples, whereas for P1–P6 samples, σ_{ics} values are more than 10 times lower than σ_{cs} values, indicating that in both samples' series the occurrence of coherent scattering (interference

Table 5 Coherent scattering cross-section (σ_{cs}), incoherent scattering cross-section (σ_{ics}), absorption cross-section (σ_A), and total cross-section (σ_T) of all (i) S1–S5 and (ii) P1–P6 glasses for thermal neutron attenuation

Glass code	σ_{cs}	σ_{ics}	σ_A	σ_T
(i) S1–S5 glasses				
S1	0.254324532	0.001644177	0.08351272	0.33948143
S2	0.263411821	0.001596485	0.080557339	0.345565645
S3	0.268869919	0.001561705	0.078439917	0.348871541
S4	0.27526077	0.001532757	0.076617759	0.353411285
S5	0.28304739	0.001480253	0.073436025	0.357963669
(ii) P1–P6 samples				
P1	0.270369221	0.017846681	7.617826519	7.906042422
P2	0.286803683	0.017070704	7.279147065	7.583021452
P3	0.295618252	0.015856581	6.75368963	7.065164462
P4	0.303229638	0.014641275	6.228048281	6.545919193
P5	0.307609319	0.01334686	5.669177408	5.990133587
P6	0.31766409	0.012356387	5.239766867	5.569787344

All values are in cm^{-1} units

between scattered neutron waves from different scattering centers (different atoms)) is higher than incoherent scattering. Generally, hydrogen has an incoherent neutron scattering cross-section that is an order of magnitude higher than incoherent or coherent neutron scattering cross-section of any other element. In our selected samples, due to the absence of 'B' atom in all the S1–S5 glass compositions, the σ_T values (0.339–0.357 cm^{-1}) are very low in comparison with σ_T values of P1–P6 samples (7.906–5.569 cm^{-1}) that have 'B' atom in their compositions. Moreover, the P1 sample has the highest σ_T value among all the P1–P6 glasses as it contains a maximum of 4.1281 wt% boron (Table 2). Thus, comparing the B element content of all P1–P6 glasses, it can be concluded that the more the B element content in samples, the better the thermal neutron shielding features. Thus, here, the P1 sample is a promising glass for thermal neutron attenuation.

Conclusions

For comparison, five bismuth tellurite (S1–S5) and six bismuth boro-tellurite (P1–P6) glasses were selected and assessed in terms of γ-ray, fast and thermal neutron attenuation aspects by computing a wide range of parameters such as μ/ρ, Z_{eff}, N_{eff}, HVL, TVL, MFP, σ_a, σ_e, EBF, EABF, Σ_R, σ_{cs}, σ_{ics}, σ_A, and σ_T. All these parameters depend on both glass chemical composition and photon energy (selected 0.015–15 MeV range). At higher energies (10–15 MeV), an overall < 7.5% deviation was

identified between both WinXCom and MCNP5 code computed μ/ρ values. At any particular photon energy, with Bi_2O_3 content addition in place of TeO_2, and TeO_2, B_2O_3 in all chosen samples, μ/ρ and Z_{eff} values are increased, while HVL, TVL, MFP, EBF, and EABF values are decreased. Thus, the more the Bi_2O_3 addition to a sample, the higher the density it gets and the better the γ-ray attenuation it affords. With the increasing penetration depth, EBF and EABF values were increased and the observed sudden peaks at 0.02 MeV and 0.04 MeV energy in EBF and EABF curves correspond to the L1-absorption edge of 'Bi' and K-absorption edge of 'Te'. PE absorption, CS, and PP processes have shown dominance at low, medium, and high photon energy regions, respectively, and μ/ρ values' decrement with an increase in energy implies that selected glasses can absorb photons productively at lower energies. The high density (6.24 g/cm^3), high μ/ρ and Z_{eff} values, low HVL, TVL, and MFP values deduced for the P6 sample (49TeO_2–21B_2O_3–30Bi_2O_3 (mol%)) suggest it as an excellent γ-ray attenuator. Moreover, computed Σ_R values varied within the range of 0.098–0.106 cm^{-1} and 0.093–0.108 cm^{-1} for all S1–S5 and P1–P6 samples, and the obtained maximum Σ_R (= 0.108 cm^{-1}) value for sample P6 suggested its high potentiality for fast neutron attenuation. Further, due to the presence of higher content of B_2O_3 (4.1281 wt% 'B'), P1 glass has the highest 'σ_T,' and it is a better candidate for thermal neutron shielding among all chosen samples. For all samples, the presented comparison studies supply sufficient information on radiation shielding and

indicate that $49TeO_2$–$21B_2O_3$–$30Bi_2O_3$ (mol%) glass could be a better γ-ray shield and can replace Pb-based glasses in facilities such as nuclear reactors and medical radiotherapy as Pb, a high-toxic element.

Supplementary data

For all the S1–S5 and P1–P6 samples, equivalent atomic number (Z_{eq}), the ((μ_m)$_{Compton}$/(μ_m)$_{Total}$) ratio (R), and G–P fitting parameters for EBF and EABF calculations within the photon energy range of 0.015–15 MeV can be found in the Supplementary data to this article.

Acknowledgements

Compliance with ethical standards

Conflict of interest   There are no conflicts to declare. The authors declare that they have no known competing financial interests or personal relationships that could have appeared to influence the work reported in this paper.

Electronic supplementary material: The online version of this article (https://doi.org/10.1007/s10853-020-04446-4) contains supplementary material, which is available to authorized users.

References

[1] Jadiyappa S (2019) Radioisotope: applications, effects, and occupational protection. In: Rahman ROA, El-Din H, Saleh M (eds) Principles and applications in nuclear engineering—radiation effects, thermal hydraulics, radionuclide migration in the environment. IntechOpen. https://doi.org/10.5772/intechopen.79161

[2] Manjunatha HC, Sathish KV, Seenappa L, Gupta D, Raj SAC (2019) A study of X-ray, gamma and neutron shielding parameters in Si-alloys. Radiat Phys Chem 165:108414

[3] Lotti P, Comboni D, Gigli L, Carlucci L, Mossini E, Macerata E, Mariani M, Gatta GD (2019) Thermal stability and high-temperature behavior of the natural borate colemanite: an aggregate in radiation-shielding concretes. Constr Build Mater 203:679–686

[4] Bel T, Arslan C, Baydogan N (2019) Radiation shielding properties of poly (methyl methacrylate)/colemanite composite for the use in mixed irradiation fields of neutrons and gamma rays. Mater Chem Phys 221:58–67

[5] Lee C-M, Lee YH, Lee KJ (2007) Cracking effect on gamma-ray shielding performance in concrete structure. Prog Nucl Energy 49:303–312

[6] Tekin HO, Kassab LRP, Issa SAM, Bordon CDS, Guclu EEA, da Mattos GRS, Kilicoglu O (2019) Synthesis and nuclear radiation shielding characterization of newly developed germanium oxide and bismuth oxide glasses. Ceram Int 45(Part A):24664–24674

[7] Ersundu AE, Büyükyıldız M, Ersundu MÇ, Şakar E, Kurudirek M (2018) The heavy metal oxide glasses within the WO_3–MoO_3–TeO_2 system to investigate the shielding properties of radiation applications. Prog Nucl Energy 104:280–287

[8] Chanthima N, Kaewkhao J, Limkitjaroenporn P, Tuscharoen S, Kothan S, Tungjai M, Kaewjaeng S, Sarachai S, Limsuwan P (2017) Development of BaO–ZnO–B_2O_3 glasses as a radiation shielding material. Radiat Phys Chem 137:72–77

[9] Elbashir BO, Sayyed MI, Dong MG, Elmahroug Y, Lakshminarayana G, Kityk IV (2019) Characterization of Bi2O3–ZnO–B2O3 and TeO2–ZnO–CdO–Li2O–V2O5 glass systems for shielding gamma radiation using MCNP5 and Geant4 codes. J Phys Chem Solids 126:112–123

[10] El-S A, Waly GS, Al-Qous MA (2018) Bourham, Shielding properties of glasses with different heavy elements additives for radiation shielding in the energy range 15–300 keV. Radiat Phys Chem 150:120–124

[11] Dong M, Elbashir BO, Sayyed MI (2017) Enhancement of gamma ray shielding properties by PbO partial replacement of WO_3 in ternary $60TeO_2$–(40-x)WO_3–$xPbO$ glass system. Chal Lett 14:113–118

[12] Tekin HO, Sayyed MI, Manici T, Altunsoy EE (2018) Photon shielding characterizations of bismuth modified borate–silicate–tellurite glasses using MCNPX Monte Carlo code. Mater Chem Phys 211:9–16

[13] Kurudirek M (2017) Heavy metal borate glasses: potential use for radiation shielding. J Alloys Compd 727:1227–1236

[14] Al-Buriahi MS, Tonguc BT (2019) Study on gamma-ray buildup factors of bismuth borate glasses. Appl Phys A 125:482/1–7

[15] El-Mallawany R, Sayyed MI, Dong MG (2017) Comparative shielding properties of some tellurite glasses: part 2. J Non-Cryst Solids 474:16–23

[16] Siengsanoh K, Chaiphaksa W, Rajaramakrishna R, Chee-wasukhanont W, Kaewkhao J (2019) Radiation shielding properties of BaO:WO$_3$:Na$_2$O:B$_2$O$_3$ glass system using WinXCom program in the range of 1 keV to 100 GeV: theoretical calculation. IOP Conf Ser J Phys Conf Ser 1259:012009/1–7. https://doi.org/10.1088/1742-6596/1259/1/012009

[17] El-Mallawany RAH (2002) Tellurite glasses handbook: physical properties and data. CRC Press, Boca Raton

[18] Pye LD, Fréchette VD, Kreidl NJ (1978) Borate glasses: structure, properties, applications. Springer, Berlin, pp 617–622

[19] Kaur S, Pandey OP, Jayasankar CK, Chopra N (2019) Spectroscopic, thermal and structural investigations of Dy^{3+} activated zinc borotellurite glasses and nano-glass-ceramics for white light generation. J Non-Cryst Solids 521:119472

[20] Lakshminarayana G, Baki SO, Sayyed MI, Dong MG, Lira A, Noor ASM, Kityk IV, Mahdi MA (2018) Vibrational, thermal features, and photon attenuation coefficients evaluation for TeO$_2$–B$_2$O$_3$–BaO–ZnO–Na$_2$O–Er$_2$O$_3$–Pr$_6$O$_{11}$ glasses as gamma-rays shielding materials. J Non-Cryst Solids 481:568–578

[21] Gaafar MS, Mahmoud IS (2019) Structural investigation and interpretation of some alkali lead borate glasses as radiation shielding materials. J Aust Ceram Soc 55:865–872

[22] Abouhaswa AS, Rammah YS, Sayyed MI, Tekin HO (2019) Synthesis, structure, optical and gamma radiation shielding properties of B$_2$O$_3$–PbO$_2$–Bi$_2$O$_3$ glasses. Compos Part B Eng 172:218–225

[23] Issa SAM, Saddeek YB, Sayyed MI, Tekin HO, Kilicoglu O (2019) Radiation shielding features using MCNPX code and mechanical properties of the PbO–Na2O–B2O3–CaO–Al2O3–SiO2 glass systems. Compos Part B Eng 167:231–240

[24] Almatari M, Agar O, Altunsoy EE, Kilicoglu O, Sayyed MI, Tekin HO (2019) Photon and neutron shielding characteristics of samarium doped lead alumino borate glasses containing barium, lithium and zinc oxides determined at medical diagnostic energies. Results Phys 12:2123–2128

[25] Salama E, Maher A, Youssef GM (2019) Gamma radiation and neutron shielding properties of transparent alkali borosilicate glass containing lead. J Phys Chem Solids 131:139–147

[26] Oo HM, Kamari HM, Yusoff WMDW (2012) Optical properties of bismuth tellurite based glass. Int J Mol Sci 13:4623–4631

[27] Azuraida A, Halimah MK, Azurahanim CAC, Ishak M (2015) Gamma irradiation effect on structural and optical properties of bismuth-boro-tellurite glasses. Int J Environ Ecol Eng 9:594–598

[28] Gerward L, Guilbert N, Jensen KB, Levring H (2004) WinXCom—a program for calculating X-ray attenuation coefficients. Radiat Phys Chem 71:653–654

[29] Sayyed MI, Lakshminarayana G, Dong MG, Ersundu MÇ, Ersundu AE, Kityk IV (2018) Investigation on gamma and neutron radiation shielding parameters for BaO/SrO–Bi2O3–B2O3 glasses. Radiat Phys Chem 145:26–33

[30] Lakshminarayana G, Kumar A, Dong MG, Sayyed MI, Long NV, Mahdi MA (2018) Exploration of gamma radiation shielding features for titanate bismuth borotellurite glasses using relevant software program and Monte Carlo simulation code. J Non-Cryst Solids 481:65–73

[31] Şakar E, Özpolat ÖF, Alım B, Sayyed MI, Kurudirek M (2020) Phy-X/PSD: development of a user friendly online software for calculation of parameters relevant to radiation shielding and dosimetry. Radiat Phys Chem 166:108496

[32] Kaur P, Singh KJ, Thakur S, Singh P, Bajwa BS (2019) Investigation of bismuth borate glass system modified with barium for structural and gamma-ray shielding properties. Spectrochim Acta-A 206:367–377

[33] Akça B, Erzeneoğlu SZ (2014) The mass attenuation coefficients, electronic, atomic, and molecular cross sections, effective atomic numbers, and electron densities for compounds of some biomedically important elements at 595 keV. Sci Technol Nucl Install 2014:1–8. https://doi.org/10.1155/2014/901465

[34] ANSI/ANS-6.4.3 (1991) Gamma-ray attenuation coefficient and buildup factors for engineering materials. American Nuclear Society, La Grange Park

[35] Singh VP, Badiger NM (2015) Shielding efficiency of lead borate and nickel borate glasses for gamma rays and neutrons. Glass Phys Chem 41:276–283

[36] Sayyed MI (2016) Investigations of gamma ray and fast neutron shielding properties of tellurite glasses with different oxide compositions. Can J Phys 94:1133–1137

[37] Dong M-G, Xue X-X, Singh VP, Yang H, Li Z-F, Sayyed MI (2018) Shielding effectiveness of boron-containing ores in Liaoning province of China against gamma rays and thermal neutrons. Nucl Sci Tech 29:58/1–8